Jpn J Clin Oncol 2008;38(7)486–492
doi:10.1093/jjco/hyn049

Low-dose Craniospinal Irradiation and Ifosfamide, Cisplatin and Etoposide for Non-metastatic Embryonal Tumors in the Central Nervous System

Koichi Yasuda[1], Hiroshi Taguchi[1], Yutaka Sawamura[2], Jun Ikeda[2], Hidefumi Aoyama[1], Kenji Fujieda[3], Nobuaki Ishii[2], Masaaki Kashiwamura[4], Yoshinobu Iwasaki[2] and Hiroki Shirato[1]

[1]Department of Radiology, Hokkaido University School of Medicine, [2]Department of Neurosurgery, Hokkaido University School of Medicine, [3]Department of Pediatrics, Hokkaido University School of Medicine and [4]Department of Otolaryngology, Hokkaido University School of Medicine, Sapporo, Japan

Received February 5, 2008; accepted May 26, 2008; published online June 23, 2008

Objective: The current study was conducted to evaluate the effects of low-dose craniospinal irradiation (CSI) combined with chemotherapy on non-metastatic embryonal tumors in the central nervous system (CNS), including medulloblastoma and supra-tentorial primitive neuroectodermal tumors (ST-PNET).
Methods: All patients were treated according to the following protocol. After surgery, the patients ≤5 years old received 18 Gy and the patients >5 years old received 24 Gy CSI. The dose to the primary tumor bed was 39.6–54 Gy. Chemotherapy consisted of ifosfamide, cisplatin and etoposide (ICE chemotherapy).
Results: Sixteen patients aged 0.5–20.4 (median 6.1) years were enrolled and followed for 11–165 (median 112) months. Both 5-year actuarial overall survival (OAS) and progression-free survival (PFS) were 81% (95% confidence interval (CI): 62–100%) for the 16 patients. Both 5-year OAS and PFS were 82% (CI: 59–100%) for the patients with medulloblastoma and 80% (CI: 45–100%) for the patients with ST-PNET. Both 5-year OAS and PFS were 75% for the eight patients ≤5 years old and 88% for the eight patients >5 years old. Both 5-year OAS and PFS were 100% for six average-risk patients (3 years or older, total resection and posterior fossa) and 70% for 10 poor-risk patients (others). The median total intellectual quotient at the last follow-up was 85 (ranging from 48 to 103) in 12 patients who were followed for 3–145 (median 49) months. Eight patients received hormone replacement therapy.
Conclusion: Low-dose CSI and ICE chemotherapy may have a role as a treatment option for a subset of patients with non-metastatic embryonal tumors in the CNS.

Key words: medulloblastoma – primitive neuroectodermal tumor – chemotherapy – radiotherapy – late effect

INTRODUCTION

The standard therapy for medulloblastoma has been 35–36 Gy craniospinal irradiation (CSI) and 54–55.8 Gy to the tumor bed after surgical resection (1). A recent randomized trial has shown that a combination of pre-radiotherapy intensive chemotherapy and 35 Gy CSI was significantly better in outcome than 35 Gy CSI alone for non-metastatic medulloblastoma in terms of event-free survival and possibly overall survival (OAS) (2). However, since CSI has produced neuro-cognitive dysfunction and endocrine deficiency in young children and infants (3), dose reduction in CSI with or without chemotherapy has been tested. A total of 25 Gy of CSI was associated with the poorer outcomes in multi-institutional phase III trials with or without chemotherapy (4,5). Subset analysis, however, showed that for patients treated with radiotherapy alone, event-free survival at

Presented in part at the 49th annual meeting of the American Society of Therapeutic Radiology and Oncology in October 2007.

For reprints and all correspondence: Koichi Yasuda, Hokkaido University School of Medicine, North-15 West-7, Kita-ku, Sapporo, Japan.
E-mail: kyasuda@radi.med.hokudai.ac.jp

© The Author (2008). Published by Oxford University Press. All rights reserved.

5 years was identical between 25 and 35 Gy CSI (4). Pilot studies and a multi-institutional phase II study suggested that 23.4–30 Gy CSI with pre- or post-radiation chemotherapy could achieve similar results with standard-dose CSI for average-risk medulloblastoma (6–8). Important questions remain with respect to the radiotherapy dose in CSI for medulloblastoma. To reduce the incidence of the late adverse effects of CSI, we performed a prospective protocol study using reduced-dose CSI sandwiched between chemotherapy that consisted of an ifosfamide, cisplatin and etoposide (ICE) regimen.

Patients with supra-tentorial primitive neuroectodermal tumors (ST-PNET) have clinical features different from those with medulloblastoma (9–12). However, these two diseases were categorized as the embryonal tumors in the WHO classification of brain tumor (9). Because of the similarity in pathological features, these two diseases have been often treated similarly (13,14). We have also determined the treatment strategy for ST-PNET to be similar to that of medulloblastoma with regard to maximal surgical resection, intensive chemotherapy and radiotherapy. Patients with ST-PNET were also entered and evaluated in this study.

In this study, we have evaluated long-term outcome, both in survival and adverse effect of patients with non-metastatic medulloblastoma and ST-PNET, or embryonal tumors in the central nervous system (CNS).

MATERIALS AND METHODS

Selection Criteria

Entry criteria for patients were as follows: the age between 6 months and 30 years, and with histologically proven medulloblastoma or ST-PNET. The patients or guardians had to give informed consent prior to surgery and again prior to adjuvant therapy.

Treatment

The flow chart of the treatment strategy is shown in Fig. 1.

Total surgical resections were attempted in patients with medulloblastoma who had Chang's Stage T1, T2 or T3a without evidence of metastasis (Stage M0) (15). Brainstem origin tumors were biopsied or partially removed. Patients with ST-PNET without evidence of metastasis were also treated at first with maximum surgical resection. Ventriculostomy, but not venticuloperitoneal shunting, was performed at tumor removal in patients with hydrocephalus.

Patients with either medulloblastoma or ST-PNET received ICE chemotherapy and CSI with a generous local boost to the tumor site (16). The ICE regimen consisted of three agents; ifosfamide at 900 mg/m^2 (Days 1–5), cisplatin at 20 mg/m^2 (Days 1–5) and etoposide at 60 mg/m^2 (Days 1–5) every 4 weeks. To prevent hemorrhagic cystitis and to suppress emesis, sodium 2-mercaptoethane sulfonate (810 mg/m^2/day) and granisetron hydrochloride (40 or 80 mg/kg/day), a 5-hydroxy-tryptamine receptor antagonist, were intravenously administered from Day 1 to 5. Hydration, including the infusion of mannitol, was done routinely.

In principle, the ICE chemotherapy regimen should have begun within 2 weeks of the surgery. The intent was for the ICE chemotherapy regimen to begin within 2 weeks of the surgery, but this did not always occur, as the timing of the chemotherapy and radiotherapy varied. Patients <2.5 years old received eight cycles of chemotherapy every 4 weeks and then received 18 Gy CSI and a local boost of 30–36 Gy when they became 2.5 years old. For patients between 2.5 and 5 years old, one course of ICE followed by 18 Gy CSI and a local boost of 30–36 Gy were scheduled. For patients <5 years old, one course of ICE followed by 24 Gy CSI and a local boost of 30 Gy were scheduled. Thus, the irradiation dose to the hypophysis and hypothalamus was 18 Gy for patients 5 years old or younger and 24 Gy (20–30) for patients >5 years in medulloblastoma. For patients with ST-PNET, the dose to the hypophysis and hypothalamus was distributed from 18 to 38 Gy.

After the radiotherapy, up to six cycles of ICE was administered to the patients 2.5 years old or older. The intent was for patients to receive CSI immediately followed by the local tumor boost, but if myelosuppression had been prolonged by the ICE before radiotherapy, they received local irradiation first, followed by CSI.

Whole-brain irradiation was performed using nearly parallel-opposed lateral fields with multi-leaf collimators to block the lenses of both eyes and including all cerebrospinal fluid space. Whole-spinal irradiation was performed using posterior single or two serially arranged posterior fields including all cerebro-spinal fluid space leaving the patient in the same position on the table. Dose distribution was calculated using a three-dimensional radiotherapy planning

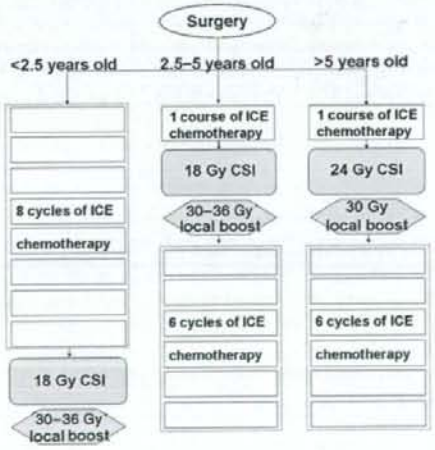

Figure 1. Flow chart of the treatment strategy. ICE chemotherapy, ifosfamide, cisplatin and etoposide; CSI, craniospinal irradiation

system. The radiotherapy dose was prescribed at the center of the midline for the whole brain and at the mean depth of the spinal canal. The boost to the posterior fossa in medulloblastoma and to the tumor bed in ST-PNET was performed using two angled and wedged fields to reduce the dose to the ear structures, temporal and posterior lobes for medulloblastoma. In patients treated in the latter half of the study period, three or more non-coplanar fields were used to reduce unnecessary dose to the surrounding structures. Daily fractions of 1.8–2.0 Gy were used at the isocenter.

Toxicity-related Dose Adjustment for the ICE Regimen

All patients underwent urological and audiological examination and renal monitoring before each cycle of chemotherapy. The chemotherapy doses were modified if there was any evidence of hematological, renal or audiological toxicity according to the dose-reduction criteria (16). If the creatinine clearance was <70%, cisplatin was omitted for that cycle and only given thereafter if renal or hearing function improved. Routine urological examination was performed from Day 1 to 5 in each cycle. Ifosfamide was omitted if macrohematuria was observed and was begun again when microscopic hematuria disappeared. Etoposide and ifosfamide were reduced according to the myelosuppression score consisting of the blood count nadir and symptoms related to the previous course of ICE (16). The score was cumulative overall courses. When using this method, the next cycle would be omitted if the score was higher than anticipated for a long time without recovery.

Follow-up

Patients were followed-up by regular clinical examination. The follow-up intervals after the end of the treatment were every month in the first year, every 3 months in the second year, every 4 months in the third year and subsequently every 6 months. Repeat cranial MRIs with or without spinal MRI were performed every 3 months in the first year and every 6 months in the second to fifth years. After that, the follow-up was performed annually at our institution or at local hospitals.

Statistical Methods

The final analysis was performed in March 2007. OAS and PFS were analyzed. OAS was calculated as the time from the date of surgical diagnosis to the date of death. Patients still alive were censored at date last seen. Subjects with average risk included children >3 years of age with posterior fossas and those with tumors that were totally or 'nearly totally' ($\leq$1.5 cc of residual disease) resected. Subjects with poor risk included children <3 years of age and/or those with subtotal resection ((1.5 cc's residual disease) and/or a non-posterior fossa location, including supra-tentorial location (10,11,12,17,18).

PFS was calculated as the time from the date of surgery to the date of recurrence or death. In those cases where death followed recurrence, the date of recurrence was used. Kaplan–Meier survival curves were produced, and log-rank tests were performed to compare OAS. Greenwood's formula was used to calculate the standard errors, which were then used to calculate the CI. The *t*-test was used to compare the interval between surgery and radiotherapy between groups.

RESULTS

Sixteen patients aged 0.5–20.4 (median 6.1) years were enrolled and followed for 11–165 months with a median of 112 months. The characteristics of the patients are listed in Table 1. In total, both the 5-year actuarial OAS and PFS were 81% (95% confidence interval, CI: 62–100%) for the 16 patients (Fig. 2). Both 5-year OAS and PFS were 82% (CI: 59–100%) for patients with medulloblastoma and 80% (CI: 45–100%) for patients with ST-PNET. The 5-year OAS and PFS were both 100% (CI: 100–100%) for the six average-risk patients and 70% (CI: 42–98%) for the 10 high-risk patients (Fig. 3). There was no statistical difference between the two groups (OAS: $P = 0.35$; PFS: $P = 0.26$). OAS and PFS were 81% (CI: 62–100%) and 68% (CI: 44–99), respectively, at 7 years, and were 74% (CI: 53–96%) and 68% (CI: 44–99%), respectively, at 9 years.

All eight patients $\leq$5 years of age received 18 Gy CSI. One of these eight patients (No. 10) experienced dissemination of the disease at 11 months after surgery and died at 16 months after surgery. Another patient (No. 11) who underwent a biopsy followed by three courses of chemotherapy and radiotherapy died at 11 months after biopsy without disappearance of the disease. The other six patients are alive at 117–months after surgery without evidence of disease. The 5-year OAS and PFS for the eight patients were both 75% (CI: 45–100%).

In the eight patients >5 years old, 24 Gy CSI was given to six patients. The CSI was stopped at 20 Gy due to severe myelosuppression in one patient (No. 4), and an additional 6 Gy (i.e. 30 Gy CSI) was given to another patient (No. 7) because of a strong fear that surgery would disseminate the disease. The 5-year OAS and PFS for the eight patients were both 88% (CI: 65–100%). Local relapse was observed in two patients, and dissemination disease was observed in one patient. All patients received 24 Gy CSI. One of them was rescued by high-dose chemotherapy with stem cell transplantation and lived for 44 months after the diagnosis of relapse. There was no statistical difference between patients $\leq$5 years and patients >5 years of age (OAS: $P = 0.51$; PFS: $P = 0.69$).

The total amounts of chemotherapeutic agents are listed in Table 2. Because we used reduction criteria for each agent in each cycle of the treatment, the total amount of chemotherapeutic agent varied. Two patients experienced relapse of the local tumor during chemotherapy, and the treatment was

Table 1. The characteristics of patients

No.	Sex	Age (years)	Primary	T	Risk	Surgery	Interval (days)	CSI (Gy)	Local (Gy)	TTT (days)	Relapse (months × 1)	Survival (months × 1)	Status	Adverse effects (months × 2)	IQ(initial) × 3	IQ (last follow-up) × 4
1	M	0.5	Cerebellum	T2	High	Partial	584	18	39.6	63		127	Alive	Growth hormone deficiency (38) Thyroid hormone deficiency (18) Radiation-induced hemangioma (53)	92	100
2	M	1	Cerebellum	T3b	High	NT	275	18	48	125		165	Alive		98	74
3	F	5	Cerebellum	T2	Low	NT	45	18	48	245		143	Alive		101	92
4	M	7.2	Cerebellum	T2	Low	NT	21	20	50	53		103	Alive	Thyroid hormone deficiency (31)	103	—
5	M	7.6	Cerebellum	T2	Low	NT	40	24	50	43	Local (76)	120	Dead	Corticosteroid deficiency (82) Thyroid hormone deficiency (49)	85	78
6	F	8.8	Cerebellum	T2	Low	Total	6	24	54	45		95	Alive	Thyroid hormone deficiency (12)	94	96
7	F	12.6	Cerebellum	T3a	Low	Total	37	30	54	49		113	Alive	Thyroid hormone deficiency (33)	68	73
8	M	20.4	Cerebellum	T2	Low	Total	7	24	50	255		111	Alive		—	—
9	F	1.2	4th ventricle	T3a	High	Total	22	18	46	40		134	Alive	Growth hormone deficiency (38) Antidiuretic hormone (ADH) deficiency (36)	79	—
10	M	1.9	4th ventricle	T3a	High	NT	262	18	50	52	Dissemin. (11)	16	Dead		—	—
11	F	2.5	pons	T3b	High	Biopsy	64	18	54	47	Local (0)	11	Dead		—	—
12	M	1.6	lt. parietal	—	High	NT	47	18	48	42		117	Alive		103	86
13	F	2.5	lt. parietal	–	High	NT	64	18	50	64		134	Alive	Corticosteroid deficiency (57) Thyroid hormone deficiency (63) Gonadotropin deficiency (115)	58	48
14	F	10.5	rt occipital	—	High	NT	22	24	54	45	Dissemin. (72)	88	Dead	Thyroid hormone deficiency (35)	—	—
15	F	12.3	rt. temporal	—	High	NT	28	24	54	49	Local (22)	28	Dead		85	—
16	M	14.3	rt occipital	—	High	NT	33	24	54	55		70	Alive		85	—

T, T stage; Interval, interval between surgery and radiotherapy; NT, nearly total resection; CSI, cerebrospinal irradiation dose; Local, local total irradiation dose; TTT, total treatment time; dissemin., dissemination; months × 1, months from surgical diagnosis; months × 2, months from the completion of all therapy at the onset of the disease or the start of hormonal supplement; IQ(initial) × 3, IQ score for the first time; IQ(last follow-up) × 4, IQ score at the last follow-up if IQ test was conducted more than once.

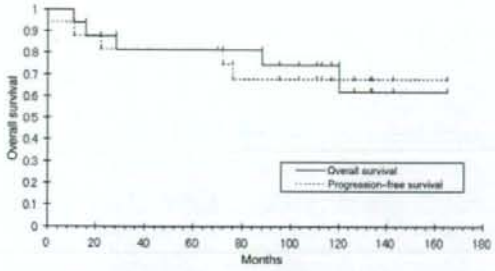

Figure 2. Overall and progression-free survival curves for 16 patients with non-metastatic embryonal tumors in the central nervous system.

stopped after three courses. The regimen of chemotherapy was changed in one patient after relapse, and a salvage operation was performed in another patient for the relapsed tumor.

Total intellectual quotient (IQ) was measured in 12 patients with the follow-up period ranging from 3 to 145 months with a median of 49 months (Fig. 4, Table 1). The median total IQ at the last follow-up was 85 (ranging from 48 to 103). In nine patients who were able to undergo the examination for verbal IQ (VIQ) and performance IQ (PIQ), there was no apparent discrepancy between VIQ (median 82, 95%CI: 48–119%) and PIQ (92, 58–113%) ($P = 0.75$). In eight patients whose total IQ was measured more than twice during the follow-up (median follow-up 78, 19–145%), two patients, whose latest IQ scores were 74 and 86, respectively, showed apparent deterioration in total IQ of >10 points (−24 and −17 points).

Eight patients received hormone replacement therapy because of deficiencies in thyroid hormone, corticosteroid hormone, growth hormone, antidiuretic hormone or gonadotropin (seven, two, two, one and one patients, respectively). Irradiated dose to the hypophysis and hypothalamus of the eight patients were 18–32 Gy (median 22 Gy). Two of the eight patients had ST-PNET.

No patients suffered from symptomatic hearing deficiency or required hearing aids. One patient experienced hemangioma in the skull in the irradiated region 4.4 years at the region which received 18 Gy and underwent surgical removal of the tumor.

Table 2. The nominal cycles of chemotherapy and the actual amount of chemotherapeutic agents

No.	Nominal cycles	Ifosfamide	Cisplatin	Etoposide
1	8	6.7	8	6.25
2	7	6.66	7	7
3	8	8	8	8
4	7	1.75	6	5.4
5	8	2	8	8
6	6	1	6	6
7	6	2.35	5.25	4.95
8	6	6	5	6
9	8	6.05	7	6.05
10	7	5.85	6	6
11	3[1]	3	3	3
12	8	4.45	5.45	6
13	8	3.95	7.2	7.2
14	6	1.75	5	4.75
15	3[1]	2.35	2.75	2.35
16	6	2.95	6	6

The dose of each agent is shown in respect of the dose for one cycle.
[1]Stopped due to relapse during the treatment.

DISCUSSION

For medulloblastoma, the results of a multi-institutional study confirmed that low-dose CSI cannot be justified with or without chemotherapy (4,5). However, the possibility of serious late complications related to radiotherapy after standard-dose CSI suggests that we should investigate better treatment options with less morbidity. Packer et al. (6) have shown that reduced-dose craniospinal radiation therapy (23.4 Gy) followed by adjuvant chemotherapy of lomustine 75 mg/m^2, vincristine 1.5 mg/m^2 and cisplatin 75 mg/m^2 for average-risk patients can achieve PFS of 79 ± 7% at 5 years for average-risk medulloblastoma. Recently, Packer et al. have conducted a phase III trial for average-risk patients in which they compared the adjuvant chemotherapy described above

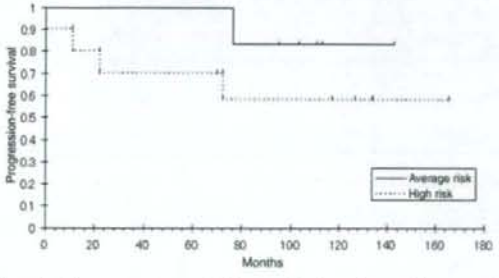

Figure 3. Progression-free survival curves for six patients with average risk and 10 patients with high risk of non-metastatic embryonal tumors in CNS.

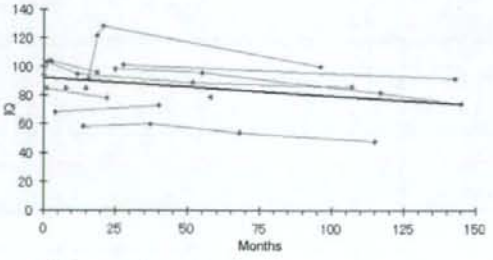

Figure 4. Temporal change of total intellectual quotient for 12 measurable patients with the regression line.

with a therapy in which cyclophosphamide was substituted for lomustine with the same low-dose craniospinal radiation therapy (23.4 Gy). They found that either choice of chemotherapy resulted in similar event-free survival rates: 82 ± 2.8% for chemotherapy with lomustine and 80% ± 3.1% for that with cyclophosphamide (19). Gajjar et al. (20) performed a prospective study of risk-adapted radiotherapy followed by chemotherapy in children with average-risk and high-risk medulloblastoma. In their analysis, 5-year event-free survival was 83% (73–93%) for the average-risk group, which received 23.4 Gy craniospinal radiotherapy, and 70% (55–85%) for the high-risk group, which received a conventional dose of 36–39.6Gy. They compared decreases in IQ and found that the difference between the low-dose craniospinal radiotherapy group and the conventional dose group was not statistically significant ($P = 0.097$) (21). The present study was consistent with their studies, showing similar survival rates and a moderate decrease in IQ. The reduced-dose CSI and chemotherapy may be as effective as standard CSI in terms of tumor control and neuro-cognitive function in long-term follow-up.

The combination of 18 Gy CSI and chemotherapy has been tested in 10 patients in a previous clinical trial, and seven of the 10 patients survived >5 years (22). Six out of eight patients ≤ 5 years old received 18 Gy CSI and survived >9 years in the present study. If we combine our results involving eight patients with these 10 patients in the literature, 13/18 survived longer than 5 years. The 5-year survival rate is not inferior to the previous results obtained with a higher CSI dose. However, Jakacki et al. (23) have reported that the administration of 1800 cGy CSI with chemotherapy to seven patients aged from 20 to 64 months was not advisable because of the high recurrence rate. Again, the number of patients was too small to exclude the possibility of a bias.

The superiority of low-dose CSI to conventional CSI for the purpose of reducing the late adverse effects remains a subject of debate (24,25). A full-scale IQ <80 was reported to be observed even in children with brain tumors who received irradiation only at the posterior fossa (26). Oyharcabal-Bourden et al. (27) have shown that the median total IQ in the follow-up was reported to be 83, and hormone replacement therapy was required in 41.9% of the patients who received adjuvant chemotherapy followed by 25 Gy craniospinal radiation therapy. Our results, which included a median total IQ of 85 and a requirement of hormone replacement therapy in 50% of the patients, were highly consistent with their study.

Treatment outcome of patients with ST-PNET has been reported to be poorer than that of those with medulloblastoma (10–11), and thus patients with ST-PNET are now treated with intensive chemotherapy in clinical trials (12). Because of the cerebral location of ST-PNET, the neuro-cognitive function is usually much poorer in these patients than in those with medulloblastoma. Our series is too small to be compared with the previous larger series, but the treatment outcome was comparable to other poor-risk patients with medulloblastoma. Careful evaluation of the long-term outcome of recent high-dose chemotherapy studies with low-dose radiotherapy for ST-PNET are warranted.

It has recently been suggested that three-dimensional conformal radiotherapy is useful for reducing the dose to the ear structures (28). Intensity-modulated radiotherapy (IMRT) was reported to reduce the dose more, but we must be careful about inducing secondary cancer due to increased whole-body irradiation by IMRT (29). The fact that one patient developed radiation-induced hemangioma in our study showed the importance of reducing unnecessary irradiation in children.

Remarkable advances in molecular biology have led us to routinely use molecular markers to select patients who would be cured with low-dose CSI and those who would respond to chemotherapy. Promeroy et al. have reported that micro-array analysis may be effective for dividing patients with medulloblastoma into favorable and unfavorable groups (30). Gajjar et al. (31) have found a possible relationship between the expression of erbB2 and PFS. Rutkowski et al. (32) have shown that the definitions of favorable and unfavorable risk groups can be improved by the determination of c-myc and trkC mRNA expression. A combined clinical and molecular staging system may well be the breakthrough to accurately predicting disease risk for patients with embryonal tumors in CNS.

The greatest shortcoming of this paper is the small number of patients. Also, combining patients with medulloblastoma and ST-PNET makes it difficult to compare our study with the previous literatures. However, the long-term follow-up of the patients in a single institution has added some potentially important findings. Our experience can be added as supplemental data suggesting a possible role for reduced-dose CSI and chemotherapy in patients with non-metastatic medulloblastoma and ST-PNET.

In conclusion, the combination of surgical resection, ICE chemotherapy and low-dose CSI may have a role in the treatment of a subset of patients with embryonal tumors in the CNS. The possibility of reducing the risk of late neuro-cognitive damage through reduction of the CSI dose is to be further evaluated.

Funding

Supported by a grain-in-aid from the Japanese Ministry of Education, Culture, Sports, Science, and Technology.

Conflict of interest statement

None declared.

References

1. Freeman CR, Taylor RE, Kortmann R, Carrie C. Radiotherapy for medulloblastoma in children: a perspective on current international clinical research efforts. *Med Pediatr Oncol* 2002;39:99–108.

2. Taylor RE, Bailey CC, Robinson K, Weston CL, Ellison D, Ironside J, et al. Results of a randomized study of preradiation chemotherapy versus radiotherapy alone for nonmetastatic medulloblastoma: the International Society of Paediatric Oncology/United Kingdom Children's Cancer Study Group PNET-3 study. *J Clin Oncol* 2003;21: 1581–91.
3. Gurney JG, Kadan-Lottick NS, Packer RJ, Neglia JP, Sklar CA, Punyko JA, et al. Endocrine and cardiovascular late effects among adult survivors of childhood brain tumors: Childhood Cancer Survivor Study. *Cancer* 2003;97:663–73.
4. Bailey CC, Gnekow A, Wellek S, Jones M, Round C, Brouwn J, et al. Prospective randomized trial of chemotherapy given before radiotherapy in childhood medulloblastoma. International Society of Paediatric Oncology (SIOP) and the (German) Society of Paediatric Oncology (GPO): SIOP II. *Med Pediatr Oncol* 1995;25:166–78.
5. Thomas PRM, Deutsch M, Kepner JL, Boyett JM, Krischer J, Aronin P, et al. Low-stage medulloblastoma: final analysis of trial comparing standard-dose with reduced-dose neuraxis irradiation. *J Clin Oncol* 2000;18:3004–11.
6. Packer RJ, Goldwein J, Nicholson HS, Vezina LG, Allen JC, Ris MD, et al. Treatment of children with medulloblastomas with reduced-dose craniospinal radiation therapy and adjuvant chemotherapy: a Children's Cancer Group Study. *J Clin Oncol* 1999;17:2127–36.
7. Kühl J, Müller HL, Berthold F, Kortmann RD, Deinlein F, Maass E, et al. Preradiation chemotherapy of children and young adults with malignant brain tumors: results of the German pilot trial HIT '88/'89. *Klin Padiatr* 1998;210:227–33.
8. Gentet JC, Bouffet E, Doz F, Tron P, Roche H, Thyss A, et al. Preirradiation chemotherapy including "eight drugs in 1 day" regimen and high-dose methotrexate in childhood medulloblastoma: results of the M7 French Cooperative Study. *J Neurosurg* 1995;82:608–14.
9. Kleihues P, Burger PC, Scheithauer BW. The new WHO classification of brain tumors. *Brain Pathol* 1993;3:255–68.
10. Cohen BH, Zeltzer PM, Boyett JM, Geyer JR, Allen JC, Finlay JL, et al. Prognostic factors and treatment results for supratentorial primitive neuroectodermal tumors in children using radiation and chemotherapy: a Childrens Cancer Group randomized trial. *J Clin Oncol.* 1995;13:1687–96.
11. Reddy AT, Janss AJ, Phillips PC, Weiss HL, Packer RJ. Outcome for children with supratentorial primitive neuroectodermal tumors treated with surgery, radiation, and chemotherapy. *Cancer.* 2000;88:2189–93.
12. Pizer BL, Weston CL, Robinson KJ, Ellison DW, Ironside J, Saran F, et al. Analysis of patients with supratentorial primitive neuroectodermal tumors entered into the SIOP/UKCCSG PNET 3 study. *Eur J Cancer.* 2006;42:1120–8.
13. Allen JC, Donahue B, DaRosso R, Nirenberg A. Hyperfractionated craniospinal radiotherapy and adjuvant chemotherapy for children with newly diagnosed medulloblastoma and other primitive neuroectodermal tumors. *Int J Radiat Oncol Biol Phys.* 1996;36:1155–61.
14. Prados MD, Edwards MS, Chang SM, Russo C, Davis R, Rabbitt J, et al. Hyperfractionated craniospinal radiation therapy for primitive neuroectodermal tumors: results of a Phase II study. *Int J Radiat Oncol Biol Phys.* 1999;43:279–85.
15. Chang CH, Housepian EM, Herbert C. An operative staging system and a megavoltage radiotherapeutic technic for cerebellar medulloblastomas. *Radiology* 1969;93:1351–9.
16. Sawamura Y, Ikeda J, Ishii N, Kato T, Tada M, Abe H, et al. Combined irradiation and chemotherapy using ifosfamide, cisplatin, and etoposide for children with medulloblastoma/posterior fossa primitive neuroectodermal tumor – results of a pilot study-. *Neurol Med Chir (Tokyo)* 1996;36:632–8.
17. Laurent JP, Chang CH, Cohen ME. A classification system for primitive neuroectodermal tumors (medulloblastoma) of the posterior fossa. *Cancer* 1985;56:1807–9.
18. Zeltzer PM, Boyett JM, Finlay JL, Albright AL, Rorke LB, Milstein JM, et al. Metastasis stage, adjuvant treatment, and residual tumor are prognostic factors for medulloblastoma in children: conclusions from the Children's Cancer Group 921 randomized phase III study. *J Clin Oncol* 1999;17:832–45.
19. Packer RJ, Gajjar A, Vezina G, Adams LR, Burger PC, Robertson PL, et al. Phase III study of craniospinal radiation therapy followed by adjuvant chemotherapy for newly diagnosed average-risk medulloblastoma. *J Clin Oncol.* 2006;24:4202–8.
20. Gajjar A, Chintagumpala M, Ashley D, Kellie S, Kun LE, Merchant TE, et al. Risk-adapted craniospinal radiotherapy followed by high-dose chemotherapy and stem-cell rescue in children with newly diagnosed medulloblastoma (St Jude Medulloblastoma-96): long-term results from a prospective, multicentre trial. *Lancet Oncol* 2006;7:813–20.
21. Mulhern RK, Palmer SL, Merchant TE, Wallace D, Kocak M, Brouwers P, et al. Neurocognitive consequences of risk-adapted therapy for childhood medulloblastoma. *J Clin Oncol* 2005;23:5511–9.
22. Goldwein JW, Radcliffe J, Johnson J, Moshang T, Packer RJ, Sutton LN, et al. Updated results of a pilot study of low dose craniospinal irradiation plus chemotherapy for children under five with cerebellar primitive neuroectodermal tumors (medulloblastoma). *Int J Radiat Oncol Biol Phys* 1996;34:899–904.
23. Jakacki RI, Feldman H, Jamison C, Boaz JC, Luerssen TG, Timmerman R. A pilot study of preirradiation chemotherapy and 1800 cGy craniospinal irradiation in young children with medulloblastoma. *Int J Radiat Oncol Biol Phys* 2004;60:531–6.
24. Ris MD, Packer R, Goldwein J, Janes-Wallace D, Boyett JM. Intellectual outcome after reduced-dose radiation therapy plus adjuvant chemotherapy for medulloblastoma: a Children's Cancer Group Study. *J Clin Oncol* 2001;19:3470–6.
25. Palmer SL, Goloubeva O, Reddick WE, Glass JO, Gajjar A, Kun L, et al. Patterns of intellectual development among survivors of pediatric medulloblastoma: a longitudinal analysis. *J Clin Oncol* 2001;19: 2302–8.
26. Grill J, Renaux VK, Bulteau C, Viguier D, Piebois CL, Rose CS, et al. Long-term intellectual outcome in children with posterior fossa tumors according to radiation doses and volumes. *Int J Radiat Oncol Biol Phys* 1999;45:137–45.
27. Oyharcabal-Bourden V, Kalifa C, Gentet JC, Frappaz D, Edan C, Chastagner P, et al. Standard-risk medulloblastoma treated by adjuvant chemotherapy followed by reduced-dose craniospinal radiation therapy: a French Society of Pediatric Oncology Study. *J Clin Oncol* 2005;23:4726–34.
28. Fukunaga-Johnson N, Sandler HM, Marsh R, Martel MK. The use of 3D conformal radiotherapy (3D CRT) to spare the cochlea in patients with medulloblastoma. *Int J Radiat Oncol Biol Phys* 1998;41:77–82.
29. Huang E, Teh BS, Strother DR, Davis QG, Chiu JK, Lu HH, et al. Intensity-modulated radiation therapy for pediatric medulloblastoma: early report on the reduction of ototoxicity. *Int J Radiat Oncol Biol Phys* 2002;52:599–605.
30. Pomeroy SL, Tamayo P, Gaasenbeek M, Sturla LM, Angelo M, McLaughlin ME, et al. Prediction of central nervous system embryonal tumor outcome based on gene expression. *Nature* 2002; 415:436–42.
31. Gajjar A, Hernan R, Kocak M, Fuller C, Lee Y, McKinnon PJ, et al. Clinical, histopathologic, and molecular markers of prognosis: toward a new disease risk stratification system for medulloblastoma. *J Clin Oncol* 2004;22:984–93.
32. Rutkowski S, von Bueren A, von Hoff K, Hartmann W, Shalaby T, Deinlein F, et al. Prognostic relevance of clinical and biological risk factors in childhood medulloblastoma: results of patients treated in the prospective multicenter trial HIT'91. *Clin Cancer Res* 2007;13:2651–7.

IOP PUBLISHING PHYSICS IN MEDICINE AND BIOLOGY

Phys. Med. Biol. **53** (2008) 2923–2936 doi:10.1088/0031-9155/53/11/011

Inference of hysteretic respiratory tumor motion from external surrogates: a state augmentation approach

D Ruan[1], J A Fessler[1], J M Balter[2], R I Berbeco[3], S Nishioka[4] and H Shirato[5]

[1] Department of Electrical Engineering and Computer Science, The University of Michigan, Ann Arbor, MI, USA
[2] Department of Radiation Oncology, The University of Michigan, Ann Arbor, MI, USA
[3] Brigham and Women's Hospital and Harvard Medical School, Boston, MA, USA
[4] Department of Radiation Oncology, NTT East Japan Sapporo Hospital, Sapporo, Japan
[5] Department of Radiation Medicine, Hokkaido University School of Medicine, Sapporo, Japan

E-mail: druan@eecs.umich.edu

Received 12 September 2007, in final form 15 April 2008
Published 6 May 2008
Online at stacks.iop.org/PMB/53/2923

Abstract

It is important to monitor tumor movement during radiotherapy. Respiration-induced motion affects tumors in the thorax and abdomen (in particular, those located in the lung region). For image-guided radiotherapy (IGRT) systems, it is desirable to minimize imaging dose, so external surrogates are used to infer the internal tumor motion between image acquisitions. This process relies on consistent correspondence between the external surrogate signal and the internal tumor motion. Respiratory hysteresis complicates the external/internal correspondence because two distinct tumor positions during different breathing phases can yield the same external observation. Previous attempts to resolve this ambiguity often subdivided the data into inhale/exhale stages and restricted the estimation to only one of these directions. In this study, we propose a new approach to infer the internal tumor motion from external surrogate signal using state augmentation. This method resolves the hysteresis ambiguity by incorporating higher-order system dynamics. It circumvents the segmentation of the internal/external trajectory into different phases, and estimates the inference map based on all the available external/internal correspondence pairs. Optimization of the state augmentation is investigated. This method generalizes naturally to adaptive on-line algorithms.

(Some figures in this article are in colour only in the electronic version)

1. Introduction

Respiratory motion affects tumors in the thorax and abdomen. In particular, breathing is the major reason for intrafractional tumor motion for lung cancer patients. It is important to

0031-9155/08/112923+14$30.00 © 2008 Institute of Physics and Engineering in Medicine Printed in the UK

monitor such motion during radiotherapy treatment to ensure the accurate delivery of radiation dose in motion-compensated intensity modulated radiotherapy (IMRT). Fluoroscopic imaging or portal imaging can monitor tumor motion during the treatment process. To reduce x-ray exposure, hybrid tumor tracking approaches that combine episodic radiographic imaging and continuous external surrogates have been investigated widely (Ozhasoglu and Murphy 2002, Murphy 2004, Murphy *et al* 2002, Schweikard *et al* 2000, 2004). Using external surrogates to infer internal tumor motion assumes that there is consistent relationship between the internal and external motions.

Hysteresis is typical in lung tumor movements, with the tumor taking a different path during inhale and exhale. Inhalation normally takes longer than exhalation, and the deflating lung volume exceeds the inflating volume at the same trans-pulmonary pressure (Keall *et al* 2006). Respiratory hysteresis makes inferring internal tumor locations from external surrogate signals challenging. Most of the external surrogate systems, such as thermistors, thermocouples, strain gauges, pneumotachographs (Kubo and Hill 1996) and infrared skin markers as applied in the Varian Real-time Position Management™ (RPM) system (Varian Medical Systems, Palo Alto, CA), provide one-dimensional signals, whose instantaneous amplitude (or displacement) alone does not provide sufficient information about the specific breathing stages.

Previous studies about correspondence between the internal tumor motion and external surrogates can be classified into two categories. One class of studies investigates the correlation between the two signals to justify the feasibility of using certain types of surrogates, or compare different surrogate options (including the placement mechanism) (Wade 1954, Vedam *et al* 2003, Ahn *et al* 2004, Hoisak *et al* 2004, Tsunashima *et al* 2004, Koch *et al* 2004, Mageras *et al* 2004). Alternatively, some other studies assume *a priori* the existence of a strong correlation between the internal and external signals, and aim to estimate the correspondence map (Seppenwoolde *et al* 2007). We adopt the latter perspective and study with a general setup the correspondence maps that take the external surrogate trace as the input and output estimates of the internal tumor location, including, but not restricted to linear relations as reflected by the correlation coefficient and its variants. The presence of respiratory hysteresis makes this a challenging problem, as the same external surrogate position can reflect different internal tumor locations during different phases. Existing methods address hysteresis by first separating empirically the breathing trajectories into two distinct 'directions' (inhale versus exhale), and then constructing a piecewise phase-dependent map (Seppenwoolde *et al* 2002, 2007, Low *et al* 2005, Lu *et al* 2005). However, subdividing the breathing into inhale and exhale phases often requires manual intervention, and is infeasible for real-time application, because a breathing 'peak' or 'trough' can only be identified retrospectively.

In this study, we propose to use a simple state augmentation of the external surrogate signal. Augmenting the state space with self-delayed observation bestows the model with 'memory', which is an alternative way to characterize the 'path-dependence' property of hysteretic systems. This procedure captures system dynamics, and embeds the breathing-phase information implicitly into the framework. We then provide the solution to a general class of parametric inference models with the augmented observations. As special cases, we derive optimal solutions for the parameters of linear and quadratic correspondence models. Furthermore, given a training internal/external dataset, we demonstrate a computationally efficient approach to choose a patient-specific (or fraction-dependent) augmentation scheme. Generalization to adaptive correspondence models follows naturally. We test the proposed approach on synchronized recordings of internal gold marker trajectories and external fiducial marker locations (Berbeco *et al* 2005).

Table 1. Description of study participants. Patients 1–3 were brought in for data acquisition purposes only, so there is no prescription dose. Patient 5 was treated twice at the same site, with two months between treatments. The tumor site is indicated using the common anatomical notation for lung segmentation: S1-3 is the upper lobe, S4-5 is the middle lobe and S6-10 is the lower lobe.

Patient	Gender	Age	Tumor Pathology	No of bb's	Tumor site	Prescribed dose (Gy)	No of fractions
1	F	47	Adenocarcinoma	4	R S7	N/A	1
2	F	70	Adenocarcinoma	3	L S6	N/A	1
3	F	71	Adenocarcinoma	2	R S5	N/A	1
4	F	47	Adenocarcinoma	3	R S4	48	8
5	M	81	Squamous cell carcinoma	3	R S6b	48	4
5						40	8
6	M	61	Small cell lung cancer	3	R S10	40	8
7	M	68	Squamous cell carcinoma	3	R S6	48	4
8	M	85	Adenocarcinoma	3	R S8	48	4

Section 2 describes the clinical data used for this test, discusses the challenges caused by hysteresis in converting the external surrogate position directly to the internal tumor location and presents the proposed method. A general correspondence model is formulated with polynomial models as an example. The optimal model parameters are derived and a generalization is given to accommodate adaptivity. Section 3 reports testing results followed by discussions. Section 4 concludes this study with a brief summary.

2. Methods and materials

2.1. Data description

To study the internal/external motion correspondence, we obtained synchronized recordings of internal tumor motion trajectories and external fiducial marker locations. The paired trajectories from eight lung cancer patients were collected with a Mitsubishi real-time radiation therapy (RTRT) system at the Radiation Oncology Clinic at the Nippon Telegraph and Telephone Corporation (NTT) hospital in Sapporo, Japan. Two to four 1.5 mm diameter gold ball bearings (bb's) were implanted in or near the tumor (Shirato *et al* 2003) and these internal markers were tracked in real time with diagnostic x-ray fluoroscopy (Shirato *et al* 2000). External surrogate signals were obtained with the AZ-733 V external respiratory gating system (Anzai Medical, Tokyo, Japan) integrated with the RTRT system. It uses a laser source and a detector, both attached to the treatment couch with the beam placed orthogonal to the patient's abdominal skin surface. The device calculates the change in the surface amplitude by measuring the relative position of the reflected light (Berbeco *et al* 2005) and outputs a one-dimensional relative position measurement of the abdominal surface. The data acquisition rate for the entire system is 30 frames per second. Table 1 describes the study participants. All patients included in this analysis had the peak-to-peak marker motion greater than 1 cm. The KV fluoroscopy + Anzai system took multiple readings for each fraction from several treatment field configurations to account for obscured x-ray views as the gantry rotated. The recording lengths varied between 20 s and 250 s with an average of 82 s. There are in total 128 readings, 46 of which were longer than 100 s.

2.2. A general correspondence model

To minimize diagnostic imaging dose in IGRT systems, it is important to infer the internal tumor location from external surrogates. In principle, we could use a correspondence model

that observes a trajectory $\vec{r}$ of the scalar external surrogate r up to the time instant n to infer the three-dimensional internal tumor position $\boldsymbol{p} = (x, y, z)$. We denote the collective surrogate information available at time n as $\vec{r}(n) \triangleq \{r(m) : 0 \leqslant m \leqslant n\}$. However, it is challenging to estimate such a map that estimates the internal tumor position from the complete collection of historical surrogate data, since the length of the input variable grows to infinity as the time progresses. A more practical choice is to use some much more compact quantity $\boldsymbol{r}$ that captures sufficient information from $\vec{r}$ for inference. With internal and external motions both being smooth, it is reasonable to approximate $\boldsymbol{p}(\boldsymbol{r})$ using polynomials. Therefore, we focus on estimating a class of correspondence models that are linear in their coefficients as follows:

$$\hat{\boldsymbol{p}}(\boldsymbol{r}) = \boldsymbol{A}\boldsymbol{f}(\boldsymbol{r}), \tag{1}$$

where $\boldsymbol{f}$ is a vector function of the external surrogate $\boldsymbol{r}$; all model parameters to be optimized are contained in the coefficient matrix $\boldsymbol{A}$. In particular, two simple correspondence models, i.e. a linear model and a quadratic model introduced in Seppenwoolde *et al* (2007), are special cases of the form given in equation (1).

Linear models assume each coordinate of internal motion is affine in $\boldsymbol{r} = r(t)$. This corresponds to the case where

$$\boldsymbol{f}(\boldsymbol{r}) = \begin{bmatrix} r \\ 1 \end{bmatrix} \qquad \text{and} \qquad \boldsymbol{A} = \begin{bmatrix} b_x & c_x \\ b_y & c_y \\ b_z & c_z \end{bmatrix}. \tag{2}$$

Quadratic models map the external surrogate to each coordinate of internal motion via a quadratic relation. It can be expressed in equation (1) with

$$\boldsymbol{f}(\boldsymbol{r}) = \begin{bmatrix} r^2 \\ r \\ 1 \end{bmatrix} \qquad \text{and} \qquad \boldsymbol{A} = \begin{bmatrix} b_x & c_x & d_x \\ b_y & c_y & d_y \\ b_z & c_z & d_z \end{bmatrix}. \tag{3}$$

Expression equation (1) is linear in the model coefficients $\boldsymbol{A}$ and yields a closed-form optimal solution in the least-squared error (LSE) sense. Given N sample points $(\boldsymbol{r}_n, \boldsymbol{p}_n), n = 1, 2, \ldots, N$, the solution to the LSE problem

$$\hat{\boldsymbol{A}} = \arg\min_{\boldsymbol{A}} E(\boldsymbol{A}), \tag{4}$$

where $E(\boldsymbol{A}) = \sum_{n=1}^{N} ||\boldsymbol{p}_n - \boldsymbol{A}\boldsymbol{f}(\boldsymbol{r}_n)||^2$, is given by solving the normal equation (Luenberger 1969) and

$$\hat{\boldsymbol{A}} = \boldsymbol{P}^T\boldsymbol{F}(\boldsymbol{F}^T\boldsymbol{F})^{-1}, \tag{5}$$

where

$$\boldsymbol{F} = \begin{bmatrix} \boldsymbol{f}(\boldsymbol{r}_1)^T \\ \vdots \\ \boldsymbol{f}(\boldsymbol{r}_N)^T \end{bmatrix} \qquad \text{and} \qquad \boldsymbol{P} = \begin{bmatrix} \boldsymbol{p}_1^T \\ \vdots \\ \boldsymbol{p}_N^T \end{bmatrix}.$$

The corresponding residual is given by

$$\begin{aligned} \Delta\boldsymbol{P} &\triangleq \boldsymbol{P} - \boldsymbol{F}\hat{\boldsymbol{A}}^T \\ &= (\boldsymbol{I} - \boldsymbol{F}(\boldsymbol{F}^T\boldsymbol{F})^{-1}\boldsymbol{F}^T)\boldsymbol{P}, \end{aligned} \tag{6}$$

with the overall residual error (summed over all three dimensions) as

$$\begin{aligned} E(\hat{\boldsymbol{A}}) &= \text{trace}\{\Delta\boldsymbol{P}^T\Delta\boldsymbol{P}\} \\ &= \text{trace}\{\boldsymbol{P}^T(\boldsymbol{I} - \boldsymbol{F}(\boldsymbol{F}^T\boldsymbol{F})^{-1}\boldsymbol{F}^T)\boldsymbol{P}\}. \end{aligned} \tag{7}$$

It may be preferable to have simpler models (with fewer free parameters) over more complicated models at the cost of small sacrifice in data fitting performance. This model selection preference can be incorporated into the optimization setting by modifying the objective function as

$$\tilde{E}(\boldsymbol{A}) = E(\boldsymbol{A}) + \lambda R(\#\boldsymbol{A}), \tag{8}$$

where $\#\boldsymbol{A}$ denotes the number of free parameters in the coefficient matrix $\boldsymbol{A}$ and R is a monotonically increasing function that assigns higher costs to more complicated models. The regularization weight λ controls the tradeoff between the data fitting $E(\boldsymbol{A})$ and the preference for lower-order models. A simple example of R would be the linear function $R(\#\boldsymbol{A}) = \#\boldsymbol{A}$, which directly penalizes the number of components in $\boldsymbol{A}$; this is equivalent to the Akaike Information Criterion (Akaike 1974). Using the closed-form optimal solution equation (5) and the expression for optimal residual error equation (7) for a given fixed model structure, the modified objective function can be minimized in two layers. We say two inference models have the same *model structure* if they only differ in parameter values. It follows immediately that all models with the same structure has equal number of degrees of freedom, thus the same complexity regularization $R(\#\boldsymbol{A})$ in equation (8). Therefore, to minimizer over models of different complexity, it is natural to choose the 'best' parameter setting within each model structure (with fixed degrees of freedom thus a constant complexity penalty), and then compare across structures. Within each class, the minimizer of the complexity-penalized objective $\tilde{E}(\tilde{A})$ is the same as that of $E(\tilde{A})$, and can be solved and evaluated efficiently using the closed-form optimal solution equation (5) and expression for optimal residual error equation (7). This motivates the two-layer hierarchical algorithm shown below for finding the optimal solution within K candidate model structures $\mathcal{C} = \cup_{i=1}^{K}\{C_i\}$.

Algorithm 1. Two-layer optimization routine for solving $\hat{\boldsymbol{A}} = \arg\min \tilde{E}(\boldsymbol{A})$ (8).

```
1: Ẽ ← +∞; i_opt ← 0; Ã ← [].
2: for i = 0 to K do
3:    Choose model structure C_i from the collection of models C,
4:    Compute R_i = R(#A) for structure C_i;
5:    Compute Â_i within class C_i according to (5) and its residual error E(Â_i) from (7).
6:    if E(Â_i) + R_i < Ẽ then
7:       Ẽ ← E(Â_i) + R_i;
8:       i_opt ← i;
9:       Ã ← Â_i.
10:   end if
11: end for
```

2.3. Hysteresis and state augmentation

Conventional methods that explicitly segment the breathing process into inhale and exhale phases have their limitations, as physical phase transitions (and delays) occur continuously rather than as discrete jumps. To circumvent the intrinsic difficulty of estimating breathing phases, we study the system dynamics directly, expecting them to sufficiently convey phase information. In a discretely observed system, one usually captures the system dynamics with time-lagged samples. For the sake of simplicity and to avoid over-parameterization, we restrict this study to a single lag. The proposed method generalizes to multiple-lag models naturally.

Given a discrete-time external surrogate $r(n)$, $n = 1, 2, \ldots, N$, we augment each external surrogate state with a time τ (in discrete unit) delayed sample, i.e. $\boldsymbol{r}(n) \triangleq (r(n), r(n-\tau))$. This augmentation captures first-order system dynamics, as the difference between $r(n)$ and $r(n-\tau)$ can be regarded as a measure of the average local velocity. As $\boldsymbol{r}$ is uniquely determined by $\vec{r}$, it fits into the general formulation equation (1). We apply the methods provided in section 2.2 to estimate the coefficients for the augmented model. To demonstrate the idea, we establish a linear model that is comparable to equation (2) and a quadratic model analogous to equation (3).

The augmented linear model (in $\boldsymbol{r}$) represents each internal coordinate as a linear combination of $r(n)$, $r(n-\tau)$ and a constant offset, corresponding to

$$\hat{\boldsymbol{p}} = \boldsymbol{A}\boldsymbol{f}(\boldsymbol{r}), \qquad \text{where} \quad \boldsymbol{f}(\boldsymbol{r}) = \begin{bmatrix} r(n) \\ r(n-\tau) \\ 1 \end{bmatrix} \tag{9}$$

with a 3×3 coefficient matrix $\boldsymbol{A}$.

The augmented quadratic model (in $\boldsymbol{r}$) estimates each internal coordinate as a linear combination of $r^2(n)$, $r(n)r(n-\tau)$, $r^2(n-\tau)$, $r(n)$, $r(n-\tau)$, 1, corresponding to

$$\hat{\boldsymbol{p}} = \boldsymbol{A}\boldsymbol{f}(\boldsymbol{r}), \qquad \text{where} \quad \boldsymbol{f}(\boldsymbol{r}) = \begin{bmatrix} r^2(n) \\ r^2(n-\tau) \\ r(n)r(n-\tau) \\ r(n) \\ r(n-\tau) \\ 1 \end{bmatrix} \tag{10}$$

with a 3×6 coefficient matrix $\boldsymbol{A}$.

In both cases, linearity in $\boldsymbol{A}$ results in the closed-form solution given by equation (5) with the corresponding $\boldsymbol{F}$, respectively.

2.4. Choice of lag length

The delay τ should be chosen properly, since too long a lag provides minimal local dynamic information and too short a lag makes the estimation sensitive to observation noise. For inference purposes, we desire a lag that maximally resolves the ambiguity in the estimated correspondence map. We choose the lag that minimizes the fitting error for training data:

$$\hat{\tau} = \arg\min_{\tau} E(\hat{\boldsymbol{A}}(\tau)), \tag{11}$$

with the objective function E defined in equation (4). The coefficients $\hat{\boldsymbol{A}}$ and the error E depend on τ because $\boldsymbol{f}$ contains both the current external surrogate displacement $r(n)$ and its lagged state $r(n-\tau)$.

Equations equation (6) and equation (7) provide a closed-form expression for $E(\hat{A}(\tau))$ for each given τ. The optimization problem equation (11) simplifies to a simple one-dimensional line search that we solve by searching over an interval with the corresponding delay time between 0 (no lag) and about half of an average breathing period.

2.5. Adaptivity of the correspondence map

Adaptivity may be useful to accommodate gradual changes in the correspondence models, due to drifting or variations in patients' breathing. In the case of linear and quadratic models, the operation in equation (5) involves inverting fairly small matrices (3×3 and 6×6, respectively),

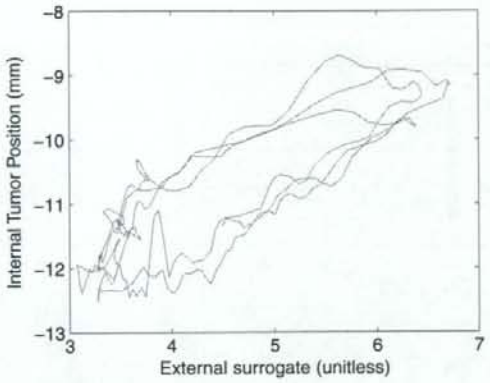

Figure 1. Example of a breathing trajectory with respiratory hysteresis.

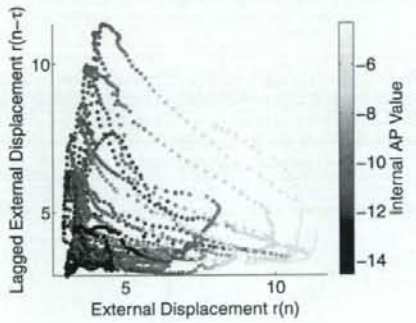

Figure 2. Scatter plot showing the data samples in augmented external state space with the colors indicating internal AP value. Locally consistent colored samples suggests the potential of resolving hysteretic ambiguity by distinguishing among different respiratory phases implicitly with state augmentation.

so direct inversion is numerically feasible. However, when more complicated models with higher degrees of freedom are used, it is desirable to reduce computation by applying recursive algorithms that modify current estimates based on newly available data. The key to recursively updating equation (5) is to avoid recomputing $(\boldsymbol{F}^T\boldsymbol{F})^{-1}$ from scratch every time. This is effectively the inversion of empirical correlation matrix with the observation $\boldsymbol{f}_i$. (Ruan *et al* 2008) provide rank-one update equations for sliding window and exponential discount adaptivities.

3. Results and discussions

To illustrate the challenges caused by hysteresis, figure 1 shows an example of the relationship between the internal tumor location obtained by fluoroscopic imaging and an external surrogate from an abdominal surface measurement as described in section 2.1. We depict only the anterior–posterior (AP) coordinate against the surrogate signal, as this axis demonstrates

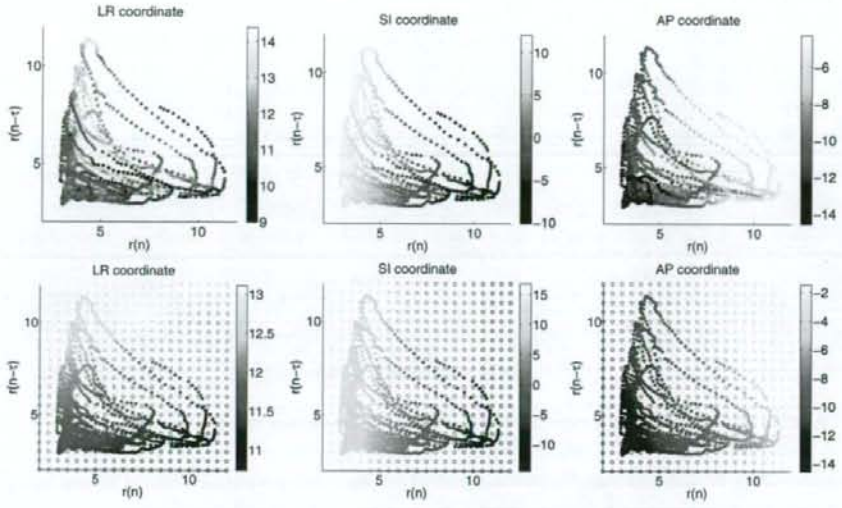

Figure 3. Correspondence relations in augmented state space and their linear fittings. Upper row: the internal tumor coordinate versus augmented state for observed samples with colors indicating internal AP value; bottom row: estimates of the tumor coordinate via linear fit with hollow circles depicting modeled hypersurface evaluated at regular grid points and solid circles for the evaluation at the sample locations, with colors indicating the estimated AP value.

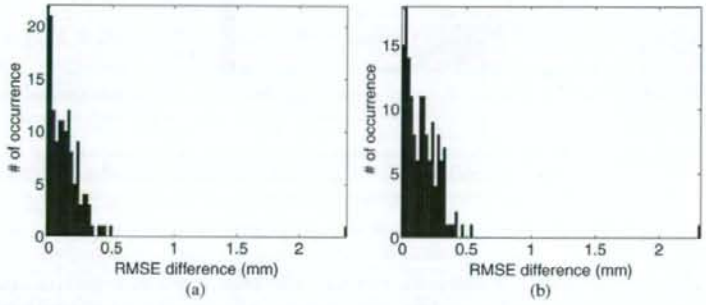

Figure 4. Histogram of paired differences between the RMS errors of the direct and augmented methods: (a) difference between the RMSE of the direct linear approach and augmented linear approach; (b) difference between the RMSE of the direct quadratic approach and augmented quadratic approach.

the strongest hysteresis for this test subject. The optimal linear and quadratic correspondence maps (Seppenwoolde *et al* 2007) provide a reasonable inference of the internal tumor motion from external surrogates, yet they fail to describe the breathing-phase dependency of an ideal correspondence map. In fact, any function that tries to map the scalar $r(n)$ to $\boldsymbol{p}$ would experience the same problem, since this is a one-to-multiple relation with hysteresis.

Figure 2 illustrates the internal tumor location in the anterior–posterior (AP) direction versus the state augmented external surrogates for $\tau = 45$, which corresponds to a 1.5 s delay

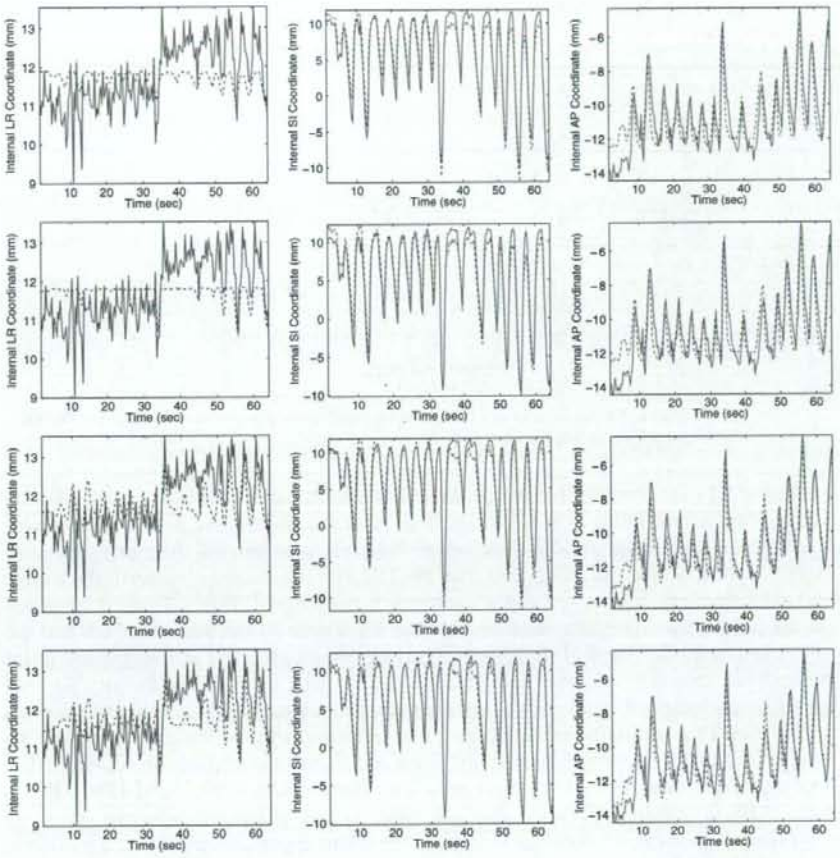

Figure 5. Estimation performance comparison among different methods. Red-solid line depicts the internal tumor position obtained from fluoroscopic imaging, and dashed-blue line provides estimated quantities from external surrogates. Each column represents one internal motion coordinate. Each row indicates the time series generated with one estimation method: (1st row) direct linear; (2nd row) direct polynomial; (3rd row) augmented linear; (bottom row) augmented polynomial.

for 30 Hz sampling rate. The scatter-plot in figure 2(a) represents each data sample in the $(r(n), r(n-\tau))$ space with a circle, and uses color (or intensity if viewed in the gray scale) to depict the internal AP coordinate values (in mm) from fluoroscopic readout. The one-to-multiple discrepancy appears largely resolved as different colored circles are not overlaid on each other, suggesting the existence of a single-valued inference map.

To illustrate the idea of model fitting in augmented state space, we first apply the simple linear model in equation (9) to the dataset shown in figure 1 with a lag length of 1.5 s (which may not be optimal), and illustrate the results in figure 3. Even though there are still noticeable differences between the observed internal coordinates in the upper row of figure 3 and their linear fit in the bottom row, the aggregated estimation error (across all patients and fractions)

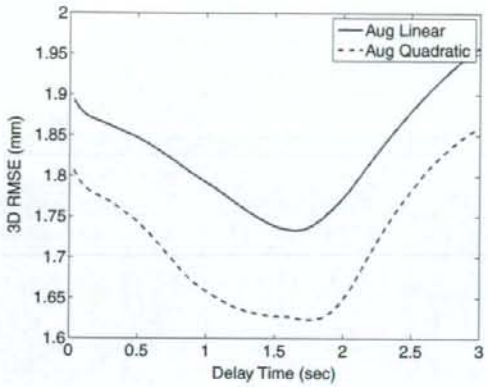

Figure 6. Estimation error as a function of lag length for state augmentation: linear fit (solid line); quadratic fit (dashed line).

reduced to 1.74 mm from 2.01 mm with direct linear fitting as in equation (2) and 1.93 mm with direct quadratic fitting as in equation (3). In particular, we observe noticeable decreases in estimation error in the AP direction, where hysteretic ambiguity is the most significant. Table 2 reports the root mean-squared error (RMSE) in each direction, respectively, for the linear and quadratic models, with and without state augmentation[6]. Figure 4 reports the paired (across patient/fraction) differences between the RMS error of the direct methods and the augmented methods. The RMSE difference between the direct linear and augmented linear methods has a mean of 0.14 mm and a median of 0.11 mm; the RMSE difference between the direct quadratic and augmented quadratic methods has a mean of 0.17 mm and a median of 0.15 mm. To assess statistical significance, we performed a paired Student's t-test with the null hypothesis that the performance of the direct and augmented methods do not differ. The p values for the linear method and the quadratic method are 4.96×10^{-13} and 4.08×10^{-18}, respectively, demonstrating that the error reductions were statistically significant.

Figure 5 shows the estimated time series of these four approaches for converting external surrogates to internal tumor locations. The higher-order models were more descriptive with the extra degrees of freedom, as demonstrated by the relative performance of quadratic models and linear models within each class respectively. State augmentation enables varying response patterns during different stages of breathing as indicated implicitly by the system dynamics.

As discussed in section 2.4, to properly choose the lag length , we use a short training set with internal–external pairs to compute offline the estimation performance $E(\hat{\boldsymbol{A}}(\tau))$ defined in equation (4) as a function of the lag length τ. In practice, the lag length does not have to be the exact optimum in equation (11); values near that optimum should sufficiently convey system dynamics. Reasonable insensitivity in the choice of lag length τ is desirable as this value is determined prior to the treatment and remains fixed subsequently. Figure 6 illustrates that the estimation error is a smooth function of the lag length, which suggests the desired robustness.

[6] For comparison purposes, we have also computed estimate from the fifth-order polynomial model with direct method, which has the same degrees of freedom (18 parameters) as the augmented quadratic model. Its estimation error is 0.75, 1.25 and 1.11 (mm) in LR, SI and AP direction respectively, with a 3D RMSE equals 1.83 mm. A paired Student's t-test between the RMSE for the fifth-order polynomial model and the augmented quadratic model yields a p-value of 1.06×10^{-10}, which indicates statistically significant error reduction by the augmented quadratic model. This shows that the improved performance of the proposed method is not a direct consequence of increased degrees of freedom, but should rather be attributed to its capability of resolving hysteretic ambiguity via state augmentation.

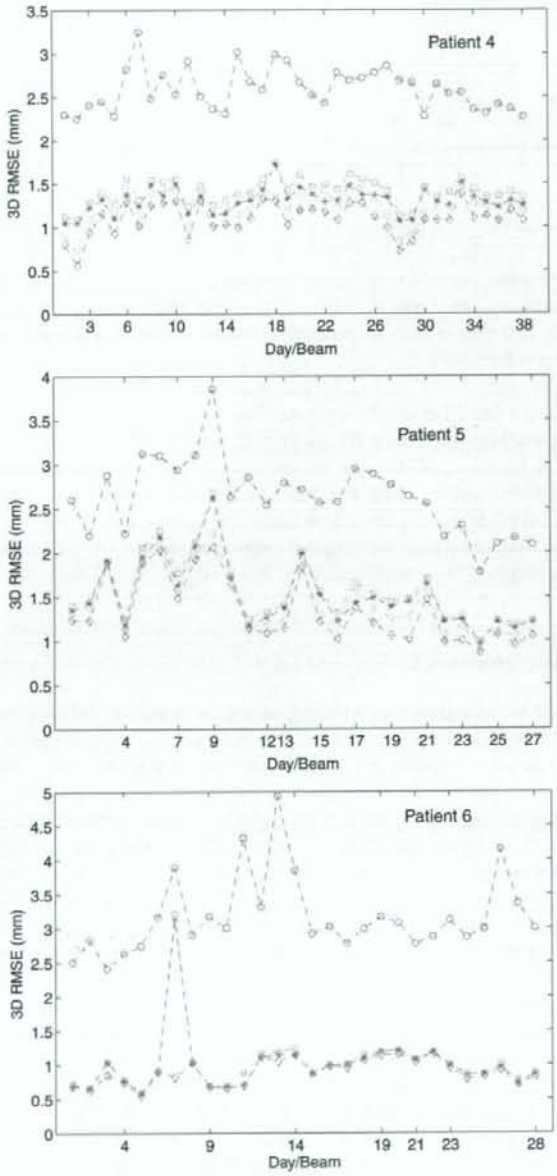

Figure 7. Beam-wise 3D RMSE (mm) for patients 4–6: minimum non-surrogate (blue circle-dashed); linear inference (green square-dashed); polynomial inference (red star-dashed); augmented linear inference (cyan triangle-dashed); augmented polynomial (magenta diamond-dashed). Non-uniform tick locations along the x-axis indicate the number of beams applied to each individual on the treatment day.

Table 2. Estimation error table.

	LR (mm)	SI (mm)	AP (mm)	3D (mm)
Direct linear	0.80	1.45	1.13	2.01
Direct quadratic	0.79	1.35	1.13	1.93
Aug. linear	0.75	1.30	0.87	1.74
Aug. quadratic	0.74	1.18	0.84	1.63

For both the linear correspondence model equation (9) and the second-order polynomial model equation (10) with state augmentation, the optimal τ corresponds to about 1.7–1.8 s delay. Without this knowledge, our previous experiments used 1.5 s delay to augment the state space (figures 2–5), and still yielded plausible results. The asymmetric slopes in figure (11) around the optimal $\hat{\tau}$ suggest that it may be preferable to use a relatively small time delay in the absence of precise information.

Assuming that the choice of lag length is robust to inter-patient and inter-fraction variations, we used a fixed lag length equivalent to 1.5 s delay for simplicity, and illustrate in figure 7 the beam-wise 3D RMSE for patients 4, 5 and 6, whose treatment extended over multiple days. The minimum RMS error for non-compensated treatment, which corresponds to a constant estimate at the retrospective mean value, is also shown for reference purposes. These results confirm that the augmented methods consistently exhibit lower error.

Adaptivity is most beneficial for irregular respiration traces. Our test data had relatively regular breathing patterns, so the inclusion of adaptivity improved the estimation accuracy only slightly.

4. Conclusion and future work

We have proposed a method to map external surrogate signals to internal tumor positions. Breathing-phase-dependent response patterns due to hysteresis are incorporated implicitly by using a simple state augmentation technique to capture system dynamics. We introduced a general class of correspondence models that are linear in model parameters, with the linear and quadratic (in external surrogate) models as special cases. We described closed-form expressions for both the optimal model parameters and the corresponding error value. Based on the latter, we further investigated the proper choice of lag length in state augmentation, and argued its relative robustness. Test results on clinical data demonstrated reduced inference error over the direct linear and polynomial models.

The number of degrees of freedom in a correspondence model determines the trade-off between flexibility and robustness. We seek a model that is descriptive enough to fit the data without undesired sensitivity to observation noise, also known as 'overfitting'. The proposed method may have more degrees of freedom than previous methods due to state augmentation. On the other hand, because it incorporates the breathing-stage information implicitly, it can use all the available internal–external correspondence pairs, without subdividing the training data as required for piecewise models (Seppenwoolde *et al* 2007, Lu *et al* 2005, Low *et al* 2005). In principle, using all the data may compensate for the possible increased sensitivity caused by the extra flexibility. The choice among different complexity levels in augmented models is still open. Both the number of augmentations and the model degree contribute to the overall complexity. Further studies should investigate methods for properly penalizing model complexity based on information criteria as explained in section 2.2.

Many research groups have observed phase shifts between external surrogate signals and internal tumor motions (Chi *et al* 2006, Ford *et al* 2003). Typically, this phase shift was to be

avoided to obtain higher internal–external correlation. However, it is possible to compensate for consistent phase shift, to simplify and improve the correspondence map estimation. In particular, we can artificially synchronize the internal–external phase by shifting one of them according to a constant offset estimated from training data. We will further study phase-offset estimation and its use in external–internal inference in the future.

This work is a preliminary study to validate the existence of a reasonably simple correspondence map and the possibility to estimate it with high accuracy. In practice, internal–external pairs are obtained at a much slower rate. Correspondence maps must be extracted from sparse imaging data and applied to continuously obtained external surrogate signals to estimate the internal tumor locations. Our method can serve as a critical module in this overall framework, yet intensive simulations and validations are further required.

Even though our test data did not exhibit dramatic improvements when using adaptive model estimation, model updates in response to changes are necessary in general. Pursuing this direction requires more thorough analysis of breathing motion variations, change detection and model adaptive rate.

Acknowledgments

We thank the reviewers for providing valuable insights and constructive suggestions in improving the quality of this work. This study is partially supported by the Barbour Fellowship at the University of Michigan and NIH grant P01-CA59827.

References

Ahn S, Yi B, Suh Y, Kim J, Lee S, Shin S, Shin S and Choi E 2004 A feasibility study on the prediction of tumor location in the lung from skin motion *Br. J. Radiol.* **77** 588–96

Akaike H 1974 A new look at the statistical model identification *IEEE Trans. Autom. Control* **19** 716–23

Berbeco R I, Nishioka S, Shirato H, Chen G T and Jiang S B 2005 Residual motion of lung tumors in gated radiotherapy with external respiratory surrogates *Phys. Med. Biol.* **50** 3655–67

Chi P M, Balter P, Luo D, Mohan R and Pan T 2006 Relation of external surface to internal tumor motion studies with cine CT *Med. Phys.* **33** 3116–23

Ford E C, Mageras G S, Yorke E and Ling C C 2003 Respiration-correlated spiral CT: a method of measuring respiratory-induced anatomic motion for radiation treatment planning *Med. Phys.* **30** 88–97

Hoisak J D, Sixel K E, Tirona R, Cheung P C and Pignol J P 2004 Correlation of lung tumor motion with external surrogate indicators of respiration *Int. J. Radiat. Oncol. Biol. Phys.* **60** 1298–306

Keall P J *et al* 2006 The management of respiratory motion in radiation oncology report of AAPM Task Group 76 *Med. Phys.* **33** 3874–900

Koch N, Liu H H, Starkschall G, Jacobson M, Forster K, Liao Z, Komaki R and Stevens C W 2004 Evaluation of internal lung motion for respiratory-gated radiotherapy using MRI: part I. Correlating internal lung motion with skin fiducial motion *Int. J. Radiat. Oncol. Biol. Phys.* **60** 1459–72

Kubo H D and Hill B C 1996 Respiration gated radiotherapy treatment: a technical study *Phys. Med. Biol.* **41** 83–91

Low D A, Parikh P J, Lu W, Dempsey J F, Wahab S H, Hubenschmidt J P, Nystrom M M, Handoko M and Bradley J D 2005 Novel breathing motion model for radiotherapy *Int. J. Radiat. Oncol. Biol. Phys.* **63** 921–9

Lu W *et al* 2005 Quantitation of the reconstruction quality of a four-dimensional computed tomography process for lung cancer patients *Med. Phys.* **32** 890–901

Luenberger D G 1969 *Optimization by Vector Space Methods* (New York: Wiley)

Mageras G S *et al* 2004 Measurement of lung tumor motion using respiration-correlated CT *Int. J. Radiat. Oncol. Biol. Phys.* **60** 933–41

Murphy M J 2004 Tracking moving organs in real time *Semin. Radiat. Oncol.* **14** 91–100

Murphy M J, Jalden J and Isaksson M 2002 Adaptive filtering to predict lung tumor breathing motion during image-guided radiation therapy *Proc. 16th Int. Congr. on Computer-assisted Radiology and Surgery* pp 539–44

Ozhasoglu C and Murphy M J 2002 Issues in respiratory motion compensation during external-beam radiotherapy *Int. J. Radiat. Oncol. Biol. Phys.* **52** 1389–99